

**Detection of applied and ambient forces with a matter-wave magnetic gradiometer**

Billy I. Robertson, Andrew R. MacKellar, James Halket, Anna Gribbon, Jonathan D. Pritchard, Aidan S. Arnold, Erling Riis, and Paul F. Griffin

*Department of Physics, SUPA, University of Strathclyde, Glasgow, G4 0NG, United Kingdom*

(Received 25 July 2017; published 16 November 2017)

An atom interferometer using a Bose–Einstein condensate of  $^{87}\text{Rb}$  atoms is utilized for the measurement of magnetic-field gradients. Composite optical pulses are used to construct a spatially symmetric Mach–Zehnder geometry. By using a biased interferometer we demonstrate the ability to measure small residual forces in our system and discriminate between magnetic and inertial effects. These are a residual ambient magnetic-field gradient of  $15 \pm 2$  mG/cm and an inertial acceleration of  $0.08 \pm 0.02$  m/s<sup>2</sup>. Our method has important applications in the calibration of precision measurement devices and the reduction of systematic errors.

DOI: [10.1103/PhysRevA.96.053622](https://doi.org/10.1103/PhysRevA.96.053622)**I. INTRODUCTION**

Matter-wave interferometry is performed by splitting the atomic wave function into two or more distinct parts, then allowing these to evolve before recombining them and performing a readout operation [1]. Alkali atoms offer an attractive medium due to the relatively simple internal structure, and the ability to readily prepare, manipulate, and interrogate them with lasers [1,2]. Atom interferometry in general offers the ability to perform precision measurements in the form of magnetic and gravitational metrology [3–10] and inertial sensing [2,10–15] as well as to test fundamental physics by making measurements of the fine-structure constant [16–19], the Newtonian gravitational constant [20], atomic polarizabilities [21], tests of the equivalence principle [22], and recent proposals for gravitational wave detection [23]. The use of Bose–Einstein condensates over thermal atoms in interferometry can be favorable due to the low atomic speed and therefore low dispersion, and increased phase coherence offering a high-contrast signal and an increased signal-to-noise ratio [9,24,25].

In this paper we present an application of atom interferometry to the measurement of magnetic- and inertial-field gradients. In the first instance we use measurements of the varying momentum-state populations at the interferometer output to measure an applied magnetic-field gradient along the interferometer axis [26]. Our apparatus is operated in two modes by using either pulsed or continuous magnetic-field gradients. We model the corresponding interferometer phases and demonstrate the effect of varying the magnitude of the gradient field as well as varying the duration of the interferometer sequence.

Through the application of bias magnetic-field gradients we further demonstrate the ability to clearly distinguish the effects of both applied and ambient magnetic and ambient inertial gradient fields. This result enables the characterization of otherwise small residual accelerating fields, both magnetic and inertial, within the complete system that would otherwise be unresolvable in an interferometer with a cosine-dependent phase sensitivity.

**II. PREPARATION OF BOSE–EINSTEIN CONDENSATE**

We load a three-dimensional (3D) magneto-optical trap (MOT) of  $\approx 10^9$   $^{87}\text{Rb}$  atoms from a two-dimensional (2D)

MOT in 15 s. After optical molasses and optical pumping into the  $|F = 2, m_F = 2\rangle$  ground state we magnetically transport our atoms horizontally to the interferometry region, 6 cm from the 3D MOT, and compress the cloud by ramping the quadrupole (QP) trap to an axial gradient of 206 G/cm. Starting with an initial phase-space density of  $10^{-6}$ , we perform radio frequency (rf) evaporative cooling by exponentially ramping a rf field from 16 to 3.4 MHz over 3 s. After this stage,  $5 \times 10^7$  atoms remain with a temperature of 32  $\mu\text{K}$ . We then adiabatically transfer the atoms into a crossed optical dipole trap over 200 ms while the rf field is ramped exponentially from 3.4 to 0.6 MHz and the QP field is ramped linearly from 206 to 15 G/cm, where the final value counteracts the acceleration due to gravity [27]. Our crossed optical dipole trap comprises two intersecting 1070 nm beams, each of 2.5 W and focused to a waist of  $w_0 = 86$   $\mu\text{m}$  positioned  $\sim 100$   $\mu\text{m}$  below the QP center. At this point we have an optical-magnetic hybrid trap containing  $\approx 4 \times 10^6$  atoms.

We continue the forced evaporative cooling by exponentially ramping the power of the dipole beams from 2.5 W to 300 mW over 4 s, and ramping the QP field from 15 to 7.5 G/cm over the first 100 ms [27]. Halfway through this stage we apply a large (20 G) bias field in the vertical direction to move the QP center up by  $\approx 2.7$  cm; this allows for a magnetic gradient with reduced curvature for use as a levitation field, in addition to a magnetic launch during a later stage of the experiment. At the end of the power ramp we hold the power constant for  $\approx 300$  ms. We now have a BEC of  $\approx 1 \times 10^5$  atoms and  $> 80\%$  purity at a temperature of  $\approx 100$  nK in the  $|F = 2, m_F = 2\rangle$  state with which we can perform interferometry. Further details on the creation of our BEC can be found in Ref. [26].

**III. INTERFEROMETER SEQUENCE**

We operate our matter-wave interferometer by using Kapitza–Dirac-type beam-splitter pulses, operating in the so-called Raman–Nath regime [1,28,29], populating atoms symmetrically in both the negative and positive momentum modes of  $|p = \pm 2\hbar k\rangle$ . In contrast to the widely used resonant-Bragg scheme, in this regime the optical pulses are provided by two laser beams of identical frequency and, hence, they provide off-resonant coupling between two-photon-coupled momentum states. However, a result of the detuned interaction is that 100% transfer to a target momentum state is not possible

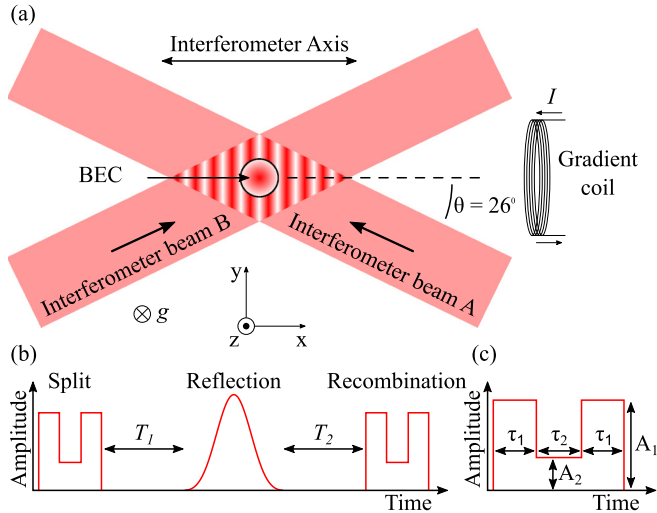


FIG. 1. (a) The interferometer beams of wavelength 780 nm cross at a half angle of  $\theta = 26^\circ$ , creating an optical lattice of period 434 nm along the  $x$  axis. We define this as our interferometer axis. The magnetic gradient coil is positioned in the  $y$ - $z$  plane and on axis with the interferometer. (b) Interferometer pulse sequence. (c). Breakdown of composite splitting and recombination pulses.

by single square pulses. To circumvent this, multipulse techniques have been proposed [30,31] and implemented [4] that show near-perfect fidelity of the beam-splitter process. These works made use of two short Kapitza–Dirac optical grating pulses, separated by a free-evolution period to allow the relative phase of the atomic momentum modes to shift by  $\pi$ , creating destructive interference in the stationary  $|p = 0\rangle$  mode. In our work we optimize the pulse parameters by numerical modeling of the Raman–Nath equations [30], with additional control over the coupling Rabi frequencies during the rephasing stage [32].

We perform interferometry by the interaction of the BEC with two laser beams of wavelength 780 nm, crossing at a half angle of  $26^\circ$  as shown in Fig. 1, and focused to a waist ( $e^{-2}$  radius) of  $w_0 \approx 95 \mu\text{m}$ . The laser is locked to the  $^{85}\text{Rb } |F = 1\rangle \rightarrow |F' = 1, 2\rangle$  crossover transition for convenience, which is  $\approx 4$  GHz blue detuned from the closest optical resonance of our BEC. The laser intensity is controlled via an acousto-optic modulator, to which we send arbitrary pulse sequences via a Stanford Research Systems DS345 arbitrary function generator. The beam is then split into two beams, A and B, and overlapped with the two arms of the crossed dipole trap as shown in Fig. 1(a). To ensure symmetric splitting, these beams are mode matched to locate the beam waist at the intersection. Both interferometer beams are vertically polarized and, as such, they drive the linear atomic Raman transitions and the atoms remain in the same internal state after each interferometer pulse. This ensures that all atoms contribute to the interferometer and avoids the blow-away pulses required in other interferometer schemes to remove untargeted states (see, e.g., Refs. [15,18]). Additionally, since the atoms in both arms are in the same internal state, the interferometer is insensitive to spatially uniform magnetic fields.

After we create our BEC we release it from the hybrid trap and allow 6 ms of mean-field expansion to reduce self-interactions [33]. Gravitational acceleration during this expansion would give a downward velocity of 59 mm/s, causing the atoms to fall out of the interferometer beams. We therefore apply a magnetic launch sequence during this time in which we ramp the levitating magnetic field from 15 to 21.8 G/cm in the first 4 ms, followed by an exponential switch-off over 2 ms. This weak positive acceleration that the atoms start above the beam center with a low downward velocity of 2 mm/s, maximizing the interferometer interrogation time. At the end of the 6 ms expansion the only field remaining is a bias field of 1.02 G in the  $z$  axis, which is used to maintain a quantization axis.

The interferometer sequence is shown in Fig. 1(b). Both interferometer beams have the same frequency and therefore produce a static optical lattice with lattice vector  $k = 2\pi \cos(\theta)/\lambda$ . We characterize the amplitude of the optical pulses in terms of recoil energy  $E_r = \hbar^2 k^2 / (2m)$ , where  $\hbar$  is the reduced Planck constant, and  $m$  is the mass of the atom. By using this metric the pulse parameters are easily transferable between atom species. We first apply a composite splitting pulse [see Fig. 1(c)] of  $\tau_1 = 26.6 \mu\text{s}$ ,  $\tau_2 = 45.6 \mu\text{s}$ ,  $A_1 = 6.07 E_r$ , and  $A_2 = 0.52 E_r$ , which separates the wave function into the  $\pm 2\hbar k$  momentum states with almost 100% efficiency, where the pulse parameters are optimized, as outlined earlier. After some time,  $T_1$ , we reverse the momenta of the wave packets by a mirror pulse with a continuous temporal profile. A Blackman pulse, with intensity profile

$$y(t) = A \left[ 0.427 - 0.497 \cos\left(\frac{2\pi(t - t_0)}{\tau}\right) + 0.077 \cos\left(\frac{4\pi(t - t_0)}{\tau}\right) \right] \quad (1)$$

for  $t_0 \leq t \leq t_0 + \tau$ , is used for the mirror sequence, because this shape has suppressed side lobes in the frequency spectrum when compared with the square pulses used in the beam splitter. Optimal parameters of a duration of  $\tau = 164 \mu\text{s}$  and amplitude  $A = 12.2 E_r$  are found from both numerical simulation and empirical optimization.

Finally, after an additional time  $T_2$ , we repeat the initial splitting pulse, which now acts to recombine the wave packets. The output of the interferometer is observed by recording an absorption image after 64 ms time of flight in a 15 G/cm magnetic levitation field to spatially separate the momentum states, and then determining the fractional populations of the  $|0\hbar k\rangle$  and  $|\pm 2\hbar k\rangle$  momentum states by fitting independent Gaussians to the integrated image profiles. The population of the  $|\pm 4\hbar k\rangle$  is negligible and therefore is not included in the normalization.

It is during the sequence of atom-optic pulses that we apply a magnetic-field gradient by passing current through a coil comprising five turns of 1-mm-diameter wire around a 2.4-cm-diameter former, positioned with the coil coaxial with the interferometer splitting axis. The separation of the center of the coil to the BEC was estimated to be  $15 \pm 1$  mm, with the uncertainty dominated by the difficulty of measuring the distance between the *in vacuo* BEC and the *ex vacuo* coil.

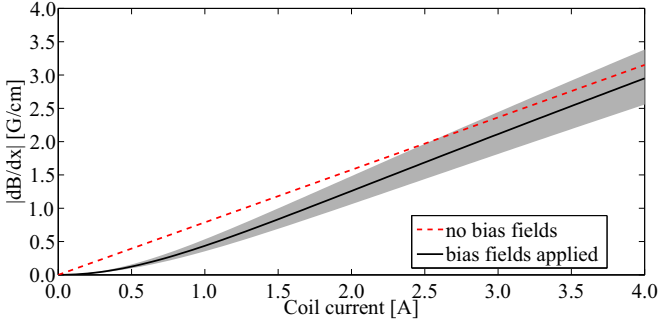


FIG. 2. Gradiometer coil model of magnetic-field gradient magnitude,  $|\partial B/\partial x|$ , vs gradiometer coil current by application of the Biot–Savart law, with (solid black line) and without (dashed red line) applied bias field of 1.02 G along the  $z$  axis. Shaded area indicates a coil position uncertainty of 1 mm.

#### IV. COIL MODEL

We create a model of the effect of our gradient coil by application of the Biot–Savart law for an on-axis current loop. We can also account for the bias field applied during the experiment that is required to maintain an atomic quantization axis, 1.02 G along the  $z$  axis, which leads to the curvature of the solid black line in Fig. 2. Note that, in the high-current regime, by which we refer to currents above 1.5 A, the effect of the bias fields diminishes and the scaling between current  $I$  and magnetic-field gradient,  $\partial B/\partial x$ , becomes approximately linear and we can write:

$$\frac{\partial B}{\partial x} = \beta(I - 0.52). \quad (2)$$

From our model we predict  $\beta = 0.85 \pm 0.11$  G/(A cm) where the uncertainty is dominated by the uncertainty in estimating the position of the coil relative to the atoms.

#### V. PULSED-MODE OPERATION

The applied magnetic-field gradient is varied by passing a current through the gradient coil. Here we operate the interferometer in pulsed mode in order to make an estimate of  $\beta$ . While the application of the aforementioned bias fields means this scaling will be slightly nonlinear at low current, as shown in Fig. 2, here we operate in the larger-current regime ( $I > 1.5$  A) where the scaling maintains a linear relationship.

Following the interferometer beam splitter, see Fig. 3(a), we apply a gradient field of duration  $\tau = 260$   $\mu$ s by passing a current through the gradient coil immediately preceding or following the reflection pulse, as indicated by the solid blue and dashed blue rectangle in Fig. 3(a), respectively. For a given interferometer duration the current through the coil is varied and the resultant fractional populations in the  $|0\hbar k\rangle$  and  $|\pm 2\hbar k\rangle$  momentum states at the output of the interferometer determined. We label the  $0\hbar k$  fractional population as  $P_{0\hbar k}$  and we plot an example of this as a function of coil current in Fig. 3, where  $T_1 = T_2 = 500$   $\mu$ s with the gradient applied before and after the reflection pulse.

The differential phase shift resulting from the temporally varying spatial separation,  $\delta x(t)$ , of the two momentum states

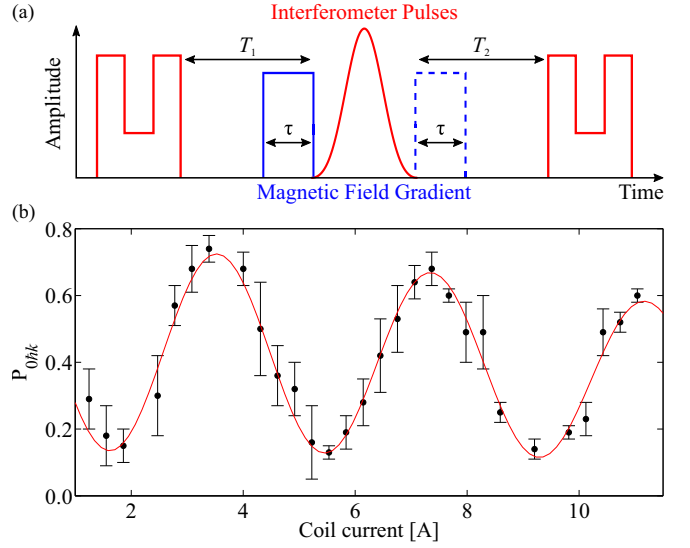


FIG. 3. (a) A gradient pulse of varying amplitude is applied before or after the reflection and an interference fringe is observed. An example fringe for  $T_1 = T_2 = 500$   $\mu$ s with the gradient pulse applied after the reflection is shown in panel (b). Error bars indicate standard deviation.

in a magnetic-field gradient can be written as [4]

$$\Delta\phi_{\text{mag}} = \int \frac{\mu \frac{\partial B}{\partial x} \delta x(t)}{\hbar} dt, \quad (3)$$

with the magnetic moment of the test atom  $\mu = m_F g_F \mu_B$  where  $m_F$  is the magnetic Zeeman level of the atom,  $g_F$  is the Landé  $g$  factor of the hyperfine atomic state, and  $\mu_B$  is the Bohr magneton. We use a simulation of the atomic trajectories to calculate the spatial separation  $\delta x(t)$ , then we numerically integrate Eq. (3) with the scaling factor  $\beta$  included in the calculation of  $\partial B/\partial x$ . This model then returns a phase,  $\Delta\phi_{\text{mag}}$ , and we fit the following equation to the data:

$$P_{0\hbar k} = A \cos(\Delta\phi_{\text{mag}} + \phi_0) G(I) + P_0, \quad (4)$$

where  $A$  is the signal amplitude and  $P_0$  is an amplitude offset. In our system the duration of the atom-optic pulses is significant with respect to the interferometer duration. As a result, the trajectories, and therefore the phase accumulation of the wave packets during the atom-optic pulses can be significant and nontrivial [32,34]. To account for this we include a phase offset  $\phi_0$  in Eq. (4). Because these pulses have occurred in the absence of a gradient field, this phase offset is the same for all gradient coil currents. We also observe a decay in the visibility of the signal for increased current and, to account for this, we include a Gaussian envelope  $G(I)$  centered around 0 A and with the standard deviation as a fit parameter. Loss of visibility at larger applied fields is attributed to acceleration effects increasing the velocity of the atomic wave packets and reducing the efficiency of the interferometer recombination pulse.

By performing interferometers with  $T_1 = T_2 = 500$   $\mu$ s, 600  $\mu$ s, and 700  $\mu$ s, we determine  $\beta = 0.79 \pm 0.01$  G/(A cm) and  $\beta = 0.81 \pm 0.01$  G/(A cm) when the gradient is applied before and after the reflection pulse, respectively. Both

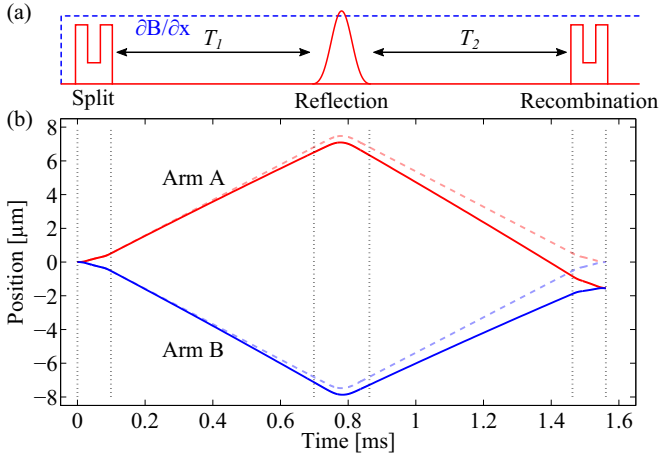


FIG. 4. (a) Red solid line shows Mach-Zehnder interferometer pulse sequence. Blue dashed line shows applied magnetic gradient. (b) Simulation of atomic trajectory in the presence of 0 G/cm (dashed lines) and 2 G/cm (solid lines) static-field gradient.

measured values of  $\beta$  are in near agreement with each other, demonstrating the symmetry of the system, and are also consistent with the predicted value.

## VI. CONTINUOUS-MODE OPERATION

### A. Theory

We now switch the interferometer to continuous-mode operation where the field gradient is applied throughout the entire interferometry sequence, as shown in Fig. 4(a). The phase difference  $\Delta\phi$  between arms A and B [Fig. 4(b)] at the output of the interferometer can be calculated by considering the classical action along each path  $S_{\text{cl}}^{\text{A}}$  and  $S_{\text{cl}}^{\text{B}}$ :

$$\Delta\phi = \frac{S_{\text{cl}}^{\text{A}} - S_{\text{cl}}^{\text{B}}}{\hbar}, \quad (5)$$

where

$$S_{\text{cl}}^{\text{A}} = \int_0^T L^{\text{A}} dt \quad \text{and} \quad S_{\text{cl}}^{\text{B}} = \int_0^T L^{\text{B}} dt, \quad (6)$$

with  $T$  being the total interferometer duration, and  $L$  being the Lagrangian which is given by the kinetic energy minus the potential energy ( $E_{\text{K}} - E_{\text{P}}$ ) [35]. For a symmetrical interferometer, such as the one reported here,  $\Delta\phi = 0$  because the phase accumulation due to the kinetic energy is equal to the phase accumulation due to the potential energy, i.e.,  $S_{\text{cl}}^{\text{A}}$  and  $S_{\text{cl}}^{\text{B}}$  are equal [35]. As a result the only phase detected in such a system is from the phase of the optical lattice produced by the splitting and recombination pulses. The positional shift caused by the gradient field results in the atoms being in a different optical potential at the point of recombination relative to the optical potential of the splitting pulse, as indicated in Fig. 4. It is therefore reasonable to consider the optical lattice as a “ruler” against which the wave-packet center of mass is measured.

The center-of-mass displacement of the BEC can be written as

$$s = \frac{\Delta\phi}{k_{\text{eff}}}, \quad (7)$$

where  $\phi$  is the phase of the interferometer output and  $k_{\text{eff}} = 4\pi \cos(\theta)/\lambda$ , where  $\lambda$  is the wavelength of the interferometry laser and  $\theta$  is the beam angle relative to the interferometry axis (see Fig. 1). Assuming zero initial velocity, the displacement can also be written as  $s = aT^2/2$ . We can therefore write

$$\Delta\phi = \frac{1}{2} a k_{\text{eff}} T^2, \quad (8)$$

with the acceleration given by

$$a = -\frac{\mu}{m} \frac{\partial B}{\partial x}, \quad (9)$$

where  $m$  is the atomic mass and  $T$  is the interferometer duration.

A simulation of the atomic trajectory is shown in Fig. 4(b) with  $\partial B/\partial x = 2$  G/cm. We also include the trajectories during the atom-optic pulses, which are determined by considering the average center-of-mass motion from simulations [32].

### B. Experiment

Here we apply the gradient for the entire interferometer duration where, due to the finite switching time of the gradient coil, we turn it on  $50 \mu\text{s}$  before the start of the splitting pulse, which will result in an initial velocity. For long interferometer durations such that  $T \gg t$ , the phase accumulation of the interferometer output will be linear with  $T^2$ , as predicted by Eq. (8). Therefore, we can write

$$P_{0\hbar k} = A \cos(k_{\text{eff}} \frac{1}{2} a T^2 + \phi_0) G(T) + P_0, \quad (10)$$

where  $A$  is amplitude, and  $P_0$  is an arbitrary amplitude offset. As above, we also observe decay in the visibility of the signal with time, and in order to obtain a good fit to the data we include a Gaussian envelope  $G(T)$  centered around  $T = 0$  with a standard deviation of 2 ms. A phase offset  $\phi_0$  is also included in the model to account for nontrivial phase evolution during the atom-optic pulses [32,34].

To test this we perform a temporally symmetric interferometer sequence of varying duration while applying a fixed gradient coil current and determine  $P_{0\hbar k}$ . We plot these data as a function of interferometer-duration squared in Fig. 5(a) and fit Eq. (10). The  $P_{0\hbar k}$  data are then converted to phase and shown in Fig. 5(b), where the straight line is the linearized version of Eq. (10).

### C. Determination of residual forces

In any apparatus designed for precision measurement it is important to characterize the system to determine any residual or unintentional forces. Here, we present a method of measuring such forces by using the atoms themselves. In our system the residual forces, and therefore accelerations, are small such that an unbiased interferometer would be insensitive to them; the signal frequency would be too low to accurately measure. Therefore, we bias our interferometer such that we can determine the magnitude and direction of a stray magnetic-field gradient as well as an inertial acceleration.

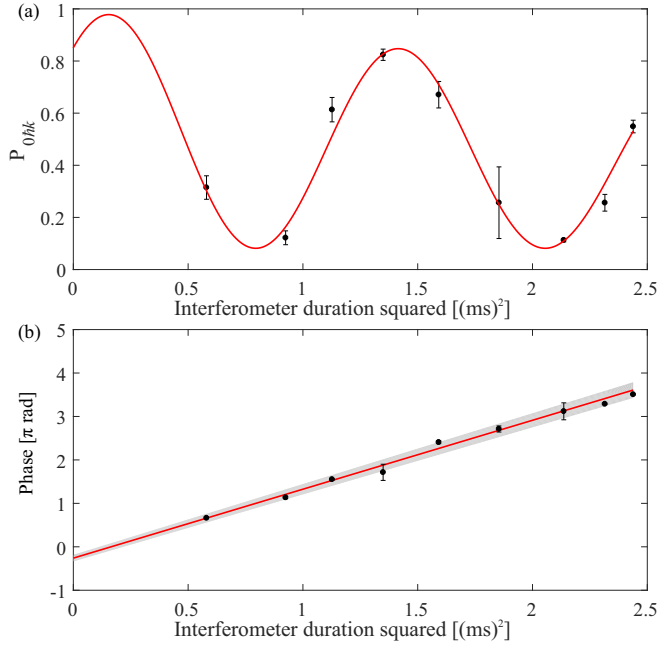


FIG. 5. (a) Gradiometer operating in continuous mode while applying a coil current of 1.9 A, with Eq. (8) fit to the data. (b) We convert population  $P_{0hk}$  to phase and fit with a linear model. The error bars indicate standard error of each data point (where not visible, these are included within the data point) while the shaded area around the straight line represents the standard deviation of the fit as a result of the uncertainty in the original fitted model. Note that the uncertainty in the phase of the data is greatly increased where the gradient of the fitted model is close to zero and for increased interferometer durations.

It should be noted that the sign of the phase shift due to magnetic fields, Eq. (3), is independent of the vector component of the magnetic field. This can be understood by recognizing that the atomic state used,  $|F = 2, m_F = 2\rangle$ , is a weak-field seeker, which will always be repelled from the coil, irrespective of the direction of current flow. This is in contrast to other inertial forces, such as gravity, that have an effect on the sign of the phase shift

$$\Delta\phi_{\text{grav}} = \int \frac{mg_x \delta x(t)}{\hbar} dt, \quad (11)$$

where the term  $g_x$  is the projection of the local acceleration due to gravity,  $g$ , onto the interferometry axis; i.e.,  $g_x = g \cos(\gamma)$ , where  $\gamma$  is the angle between the  $x$  axis and the gravitational acceleration.

In Sec. VIB we ignored the effect of the initial velocity of the atoms as a result of applying the gradient field  $t = 50 \mu\text{s}$  before the start of the splitting pulse. The rise time of the coil current has an exponential form of  $1 - \exp(-t/\tau)$  with  $\tau = 5.7 \mu\text{s}$ , and therefore  $u = at$  becomes  $u = a[t + \tau \exp(-\tau/t) - \tau]$ . This results in an effective shortening of  $t$  from 50 to 44  $\mu\text{s}$ . When we include this initial velocity, the phase accumulation of the interferometer goes as  $k_{\text{eff}}(uT + \frac{1}{2}aT^2)$ , and  $P_{0hk}$  will have the form

$$P_{0hk} = A \cos \left[ k_{\text{eff}} \left( uT + \frac{1}{2}aT^2 \right) + \phi_0 \right] G(T) + P_0. \quad (12)$$

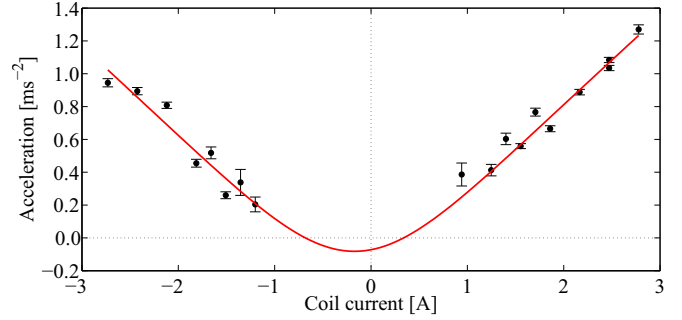


FIG. 6. Measured acceleration for varying gradient coil currents. Error bars indicate standard deviation. The fitted curve is a model of our gradient coil with coil-atom distance, acceleration offset, and current offset as free parameters. We determine the effective coil-atom distance to be  $15.0 \pm 0.2$  mm.

For a range of gradiometer coil currents we probe our system for varying interferometer durations  $T$ . To these data we fit Eq. (12) and extract an acceleration and plot the data in Fig. 6. We fit our coil model to these data with the coil distance, acceleration offset, and current offset as the free parameters. The coil distance is found to be  $15.0 \pm 0.2$  mm from the fit, in good agreement with the spatial measurement.

The residual magnetic-field gradient is determined entirely by the current offset ( $0.17 \pm 0.02$  A) of the fitted curve in Fig. 6, which is the current that cancels out the residual field. From our coil model, along with the fitted coil-atom distance we calculate the value of this field gradient to be  $15 \pm 2$  mG/cm.

Residual forces that are nonmagnetic (gravitational, electrostatic, etc.) can be determined entirely from the acceleration offset of the fitted model, where a negative offset indicates a force toward the coil and vice versa. From the acceleration offset in the fitted model we determine a residual acceleration of  $-0.08 \pm 0.02$  m/s<sup>2</sup>. If we attribute this to a tilt in the interferometer axis with respect to gravity, it is equivalent to an angle of  $\gamma = -0.5 \pm 0.1^\circ$ . The negative sign indicates that the angle of the interferometer axis with respect to gravity is such that, in the absence of an applied field, the atoms would accelerate towards the gradient coil. Without the use of this method it would be not be possible to characterize the residual forces with our interferometer in its current, horizontal implementation; in order to make a direct measurement of our residual nonmagnetic force we would require interferometer durations of  $\sim 6$  ms to observe just one complete fringe, at which time the atoms would have fallen out of the interrogation region.

For these data we are also able to extract a  $\beta$  value, and we find  $\beta = 0.81 \pm 0.02$  G/(A cm). This is consistent with our initial estimate of  $\beta = 0.85 \pm 0.11$  G/(A cm) and agrees well with our measured values of  $\beta = 0.79 \pm 0.01$  G/(A cm) and  $\beta = 0.81 \pm 0.01$  G/(A cm) from operating the interferometer in pulsed mode in Sec. V.

## VII. CONCLUSIONS

In summary, we have constructed a matter-wave interferometer and have demonstrated its ability to make measurements

of magnetic-field gradients. Two modes of operation have been demonstrated: pulsed mode and continuous mode. Both methods show good agreement in measuring the scaling factor  $\beta$  relating the gradient coil current to the magnetic-field gradient, and these values are also consistent with our initial estimate. In addition, we have created a method for measuring low ambient fields that would be impossible to measure by using an unbiased cosine-sensitive interferometer because the required interferometer durations would be too long. One can therefore envisage the measurement of even smaller ambient fields by extending the available interrogation time. In our case this would require the use of interferometry beams with a larger waist, or the use of

a magnetic levitation field, which would potentially couple noise into the system. The techniques presented provide excellent tools for the characterization of applied magnetic-field gradients and residual accelerating fields, crucial in precision measurement.

#### ACKNOWLEDGMENT

This work was funded by the UK National Quantum Technology Hub in Sensing and Metrology, through the EPSRC (EP/M013294/1).

Data associated with this work are openly available at <http://dx.doi.org/10.15129/a91463ed-e359-4614-bdf5-45e0eefe2c7d>.

- 
- [1] A. D. Cronin, J. Schmiedmayer, and D. E. Pritchard, *Rev. Mod. Phys.* **81**, 1051 (2009).
- [2] T. L. Gustavson, A. Landragin, and M. Kasevich, *Classical Quantum Gravity* **17**, 2385 (2000).
- [3] M. J. Snadden, J. M. McGuirk, P. Bouyer, K. G. Haritos, and M. A. Kasevich, *Phys. Rev. Lett.* **81**, 971 (1998).
- [4] Y.-J. Wang, D. Z. Anderson, V. M. Bright, E. A. Cornell, Q. Diot, T. Kishimoto, M. Prentiss, R. A. Saravanan, S. R. Segal, and S. Wu, *Phys. Rev. Lett.* **94**, 090405 (2005).
- [5] M.-K. Zhou, Z.-K. Hu, X.-C. Duan, B.-L. Sun, J.-B. Zhao, and J. Luo, *Phys. Rev. A* **82**, 061602 (2010).
- [6] B. Barrett, I. Chan, and A. Kumarakrishnan, *Phys. Rev. A* **84**, 063623 (2011).
- [7] A. V. Rakholia, H. J. McGuinness, and G. W. Biedermann, *Phys. Rev. Appl.* **2**, 054012 (2014).
- [8] G. Rosi, L. Cacciapuoti, F. Sorrentino, M. Menchetti, M. Prevedelli, and G. M. Tino, *Phys. Rev. Lett.* **114**, 013001 (2015).
- [9] S. Abend, M. Gebbe, M. Gersemann, H. Ahlers, H. Müntinga, E. Giese, N. Gaaloul, C. Schubert, C. Lämmerzahl, W. Ertmer, W. P. Schleich, and E. M. Rasel, *Phys. Rev. Lett.* **117**, 203003 (2016).
- [10] K. S. Hardman, P. J. Everitt, G. D. McDonald, P. Manju, P. B. Wigley, M. A. Sooriyabandara, C. C. N. Kuhn, J. E. Debs, J. D. Close, and N. P. Robins, *Phys. Rev. Lett.* **117**, 138501 (2016).
- [11] F. Riehle, T. Kisters, A. Witte, J. Helmcke, and C. J. Bordé, *Phys. Rev. Lett.* **67**, 177 (1991).
- [12] T. L. Gustavson, P. Bouyer, and M. A. Kasevich, *Phys. Rev. Lett.* **78**, 2046 (1997).
- [13] A. Lenef, T. D. Hammond, E. T. Smith, M. S. Chapman, R. A. Rubenstein, and D. E. Pritchard, *Phys. Rev. Lett.* **78**, 760 (1997).
- [14] D. S. Durfee, Y. K. Shaham, and M. A. Kasevich, *Phys. Rev. Lett.* **97**, 240801 (2006).
- [15] P. Berg, S. Abend, G. Tackmann, C. Schubert, E. Giese, W. P. Schleich, F. A. Narducci, W. Ertmer, and E. M. Rasel, *Phys. Rev. Lett.* **114**, 063002 (2015).
- [16] S. Gupta, K. Dieckmann, Z. Hadzibabic, and D. E. Pritchard, *Phys. Rev. Lett.* **89**, 140401 (2002).
- [17] A. Wicht, J. M. Hensley, E. Sarajlic, and S. Chu, *Phys. Scr.* **T102**, 82 (2002).
- [18] P. Cladé, E. de Mirandes, M. Cadoret, S. Guellati-Khélifa, C. Schwob, F. Nez, L. Julien, and F. Biraben, *Phys. Rev. A* **74**, 052109 (2006).
- [19] R. Bouchendira, P. Cladé, S. Guellati-Khélifa, F. Nez, and F. Biraben, *Phys. Rev. Lett.* **106**, 080801 (2011).
- [20] G. Lamporesi, A. Bertoldi, L. Cacciapuoti, M. Prevedelli, and G. M. Tino, *Phys. Rev. Lett.* **100**, 050801 (2008).
- [21] B. Deissler, K. J. Hughes, J. H. T. Burke, and C. A. Sackett, *Phys. Rev. A* **77**, 031604 (2008).
- [22] S. Fray, C. A. Diez, T. W. Hänsch, and M. Weitz, *Phys. Rev. Lett.* **93**, 240404 (2004).
- [23] P. W. Graham, J. M. Hogan, M. A. Kasevich, and S. Rajendran, *Phys. Rev. Lett.* **110**, 171102 (2013).
- [24] J. E. Debs, P. A. Altin, T. H. Barter, D. Döring, G. R. Dennis, G. McDonald, R. P. Anderson, J. D. Close, and N. P. Robins, *Phys. Rev. A* **84**, 033610 (2011).
- [25] Y. Torii, Y. Suzuki, M. Kozuma, T. Sugiura, T. Kuga, L. Deng, and E. W. Hagley, *Phys. Rev. A* **61**, 041602 (2000).
- [26] B. I. Robertson, Ph. D. thesis, University of Strathclyde, 2016.
- [27] Y.-J. Lin, A. R. Perry, R. L. Compton, I. B. Spielman, and J. V. Porto, *Phys. Rev. A* **79**, 063631 (2009).
- [28] E. M. Rasel, M. K. Oberthaler, H. Batelaan, J. Schmiedmayer, and A. Zeilinger, *Phys. Rev. Lett.* **75**, 2633 (1995).
- [29] S. Gupta, A. E. Leanhardt, A. D. Cronin, and D. E. Pritchard, *C. R. Acad. Sci., Ser. IV: Phys., Astrophys.* **2**, 479 (2001).
- [30] S. Wu, Y.-J. Wang, Q. Diot, and M. Prentiss, *Phys. Rev. A* **71**, 043602 (2005).
- [31] M. Edwards, B. Benton, J. Heward, and C. W. Clark, *Phys. Rev. A* **82**, 063613 (2010).
- [32] A. R. MacKellar, B. I. Robertson, J. Halket, A. S. Arnold, E. Riis, and P. F. Griffin (unpublished).
- [33] A. O. Jamison, J. N. Kutz, and S. Gupta, *Phys. Rev. A* **84**, 043643 (2011).
- [34] C. Antoine, *Phys. Rev. A* **76**, 033609 (2007).
- [35] P. Storey and C. Cohen-Tannoudji, *J. Phys. II* **4**, 1999 (1994).